

Exploring the phase diagram of InAs/GaSb/InAs trilayer quantum wells

S. Schmid,^{1,*} M. Meyer,¹ F. Jabeen,¹ G. Bastard,^{1,2} F. Hartmann,^{1,†} and S. Höfling¹

¹*Technische Physik, Physikalisches Institut and Würzburg-Dresden Cluster of Excellence *ct.qmat*, Am Hubland, D-97074 Würzburg, Germany*

²*Physics Department, École Normale Supérieure, PSL 24 rue Lhomond, 75005 Paris, France*



(Received 21 December 2021; accepted 29 March 2022; published 11 April 2022)

We study topological insulators based on InAs/GaSb/InAs trilayer quantum wells with different InAs thicknesses ranging from 8.0 to 13.5 nm to experimentally ascertain the phase diagram in this material system. Gate-voltage and temperature-dependent transport measurements reveal distinct transport signatures between samples designed from the trivial-insulating, the topological-insulating, up to the semimetallic phase. Two-carrier transport together with pronounced Van Hove singularities are observable only for the samples grown in the topological-insulating phase and if camelback-like dispersions are present in the hybridized valence or conduction band. The different shaping and the amount of Van Hove singularities in our samples deliver information about a turning point inside the topological-insulating phase. Temperature-dependent measurements allow to further confirm the gap energy values for the trivial- and topological-insulating samples. Furthermore, the indirect inverted gaps are found to be more temperature insensitive in comparison to the trivial gap.

DOI: [10.1103/PhysRevB.105.155304](https://doi.org/10.1103/PhysRevB.105.155304)

I. INTRODUCTION

Topological insulators (TI) based on the InAs/GaSb material system are especially appealing because of the spatial separation and localization of electron and hole states in the InAs and GaSb layers, respectively [1]. The spatial separation of charges provides the necessary ingredient to a rich phase diagram that is accessible and controllable by a bottom- and top-gate electrode. A dual-gating approach enables to control the electric field and the Fermi energy (E_F) independently. Therefore, TIs based on InAs/GaSb quantum wells allow tuning between the trivial- and topological phases by external control parameters [2]. Due to this electric field tunability, the advanced epitaxial growth and transport device fabrication techniques of the so-called 6.1 Angstrom family (InAs, GaSb, and AlSb), utilizing InAs/GaSb bilayer quantum wells (BQWs), have been investigated extensively in recent years [1–9]. Although the bulk gap energy in InAs/GaSb BQWs is much smaller compared to the HgTe/CdTe system [10], strain-engineered InAs/GaInSb BQWs can also reach hybridized gaps up to 35 meV [1,5,11]. Yet, this value is still smaller compared to gap energies of up to 55 meV for highly strained HgTe/CdTe QWs [12]. Interestingly, by adding a second InAs layer, i.e., by forming an InAs/GaSb/InAs trilayer quantum well (TQW), it was theoretically predicted that the indirect inverted gap could reach values up to 60 meV for strained InAs/Ga_{1-x}In_xSb/InAs TQWs [13]. Another potential advantage arises within the 6.1 Angstrom family beside the wide gate-tunability range as the gap is expected to be rather temperature insensitive [13] in contrast to the HgTe/CdTe QW system where a temperature-dependent gap closing is

observed [14,15]. The phase diagram for the TQWs can be separated into three different regions depending on the InAs and/or GaSb layer thicknesses: trivial bulk-insulating phase, TI phase, and a semimetallic phase [13]. TQWs in InAs geometry (InAs/GaSb/InAs) displaying an indirect inverted gap have been evidenced recently [16]. Furthermore, evidence for massless Dirac fermions has also been given by magneto-transport measurements [17]. Additional experimental reports suggest that the indirect inverted gap in this system is rather temperature independent [16,18,19] and TQWs with GaSb geometry (GaSb/InAs/GaSb) can even exhibit different phases, such as bilayer graphene [13].

II. EXPERIMENTAL RESULTS AND DISCUSSIONS

In this study, we evaluate the phase diagram of InAs/GaSb/InAs TQWs from the trivial-insulating, the topological-insulating, up to the semimetallic phase. We have grown and fabricated TQWs with constant GaSb layer thickness and varying InAs layer thicknesses to study the transport signatures for the different phases. For the trivial-insulating and the semimetallic phases, single-carrier transport is observed. The trivial-insulating phase shows a clear gap while the semimetallic phase is gapless as expected. By contrast in the TI phase, the hybridized band structure of TQWs leads to distinct characteristic points in the gate-voltage dependent longitudinal resistivity ρ_{xx} , the so-called Van Hove singularities (VHS). These are observable as a local minimum in ρ_{xx} if the dispersion shows a camelback-like dispersion. To reveal experimentally the values and natures of the energy gaps, temperature-dependent transport measurements have been carried out.

A schematic of the band profile of a TQW in InAs geometry is shown in Fig. 1(a). In InAs geometry, the center of the TQW is a GaSb quantum well with thickness d_2 that is

*sebastian.schmid@physik.uni-wuerzburg.de

†fabian.hartmann@uni-wuerzburg.de

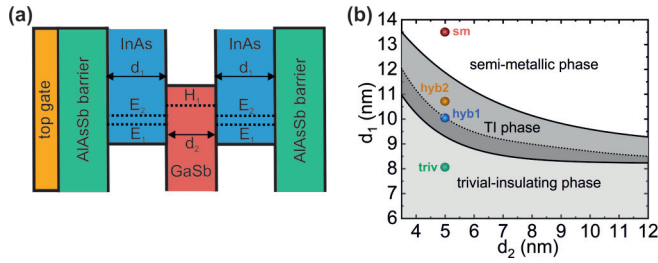


FIG. 1. (a) Schematic band structure of an inverted TQW in InAs geometry embedded in $\text{AlAs}_{0.08}\text{Sb}_{0.92}$ barriers. The layer thicknesses for both InAs and GaSb layers are given by d_1 and d_2 , respectively. The hole level H_1 is localized in the GaSb layer, while the electron levels E_1 and E_2 are located in the InAs layers. (b) Calculated phase diagram for the TQW in InAs geometry. The phase diagram displays the three different phases: trival-insulating, TI, and the semimetallic phase. The TI phase can be further divided into two subphases dependent on the position of the indirect inverted gap, i.e., H_1 - E_1 (dark gray) and E_2 - E_1 (gray). The color-coded dots mark the position of the examined samples.

sandwiched by two InAs quantum wells with thicknesses d_1 . The TQW is embedded in two barriers. The barrier material can either be the lattice-matched $\text{AlAs}_{0.8}\text{Sb}_{0.92}$ with a band gap energy of 2.323 eV [20] as it is the case for our samples or, as in most systems, the simple binary AlSb (with a band-gap energy of 2.320 eV [20]). The valence- and conduction-band offset difference between $\text{AlAs}_{0.8}\text{Sb}_{0.92}$ and AlSb is 90.8 and 94.2 meV, respectively. A full schematic on the trilayer wells embedded in AlSb barriers can be found in Ref. [13]. The highest (heavy-) hole state with energy H_1 is localized in the GaSb well. The lowest electron states E_1 and E_2 are localized in the InAs layers [13,21]. Via the quantum-well thicknesses d_1 and d_2 , TQWs exhibit a rich phase diagram with different insulating and semimetallic phases. Based on the calculations performed in Ref. [13], the numerically calculated phase diagram for TQWs with InAs geometry is shown in Fig. 1(b). The phase diagram was calculated via the 8-band $k \cdot p$ method using the NEXTNANO⁺⁺ simulation tool [22]. It exhibits three different phases: trival-insulating phase (light gray), the topological-insulating phase (gray and dark gray), and the semimetallic phase (white). The position of the maximal indirect inverted gap within the TI phase is marked with the dotted line. This line in addition marks the transition point where the topological-insulating phase can further be divided into two different subphases, as will be explained in detail later. The four examined samples, named triv, hyb1, hyb2, and sm, are marked with the four color-coded dots and the InAs layer thicknesses are $d_1 = 8.0, 10.0, 10.75,$ and 13.5 nm, respectively. For all samples the GaSb thickness is constant at $d_2 = 5.0$ nm.

In Fig. 2 the simulated band dispersion for the four color-coded points in the phase diagram are shown. Figure 2(a) displays the band dispersion for the sample in the trival-insulating phase with trivial band ordering. The H_1 level lies energetically below E_1 and E_2 . Figure 2(b) displays the band dispersion of the gapless semimetallic phase, obtained for large d_1 (sm TQW). For intermediate InAs layer thicknesses, the band ordering is nontrivial. Figures 2(c) and 2(d) show

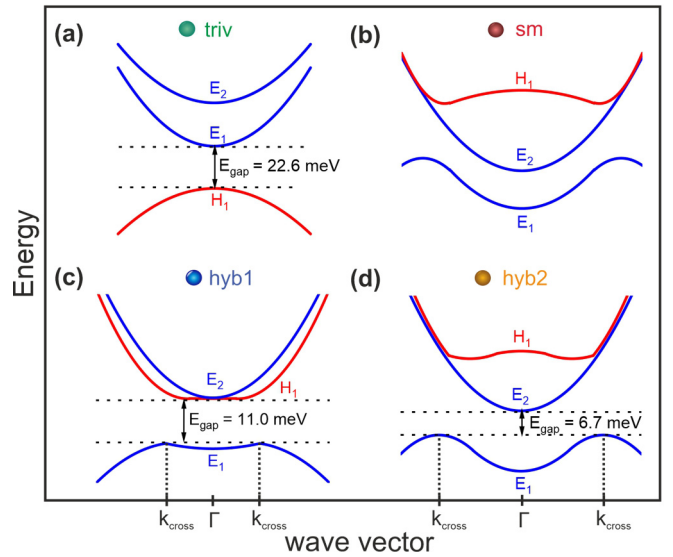


FIG. 2. Calculated band dispersions for a constant GaSb thickness $d_2 = 5.0$ nm and InAs thicknesses $d_1 = 8.0, 13.5, 10.0,$ and 10.75 nm in (a), (b), (c), and (d), respectively. On the x axis, the Γ point for all dispersion is shown. Additionally, the crossing points for (c) and (d) where $k = k_{\text{cross}}$ are highlighted. (a) In the trival-insulating phase, E_2 and E_1 are energetically above H_1 and the band ordering is trivial. The band-gap energy has a value of 22.6 meV. (b) In the semimetallic phase, the minimum of the conduction band is energetically below the maximum of the valence band leading to a gapless state. (c) For hyb1, E_1 lies energetically below H_1 . A camelback-like dispersion is observed where the local minimum of the valence band lies below the maximum of the valence band. In the conduction band, a weak camelback-like dispersion is present. The indirect inverted gap has a value of 11.0 meV. (d) For hyb2, E_2 , and E_1 lie below H_1 leading to a pronounced camelback for the E_1 subband while E_2 remains parabolic. The indirect inverted gap has a value of about 6.7 meV.

the dispersion relations for the hyb1 and the hyb2 sample. In Fig. 2(c) the E_2 -band minimum is located at the local maximum of the H_1 band. The indirect inverted gap (E_{gap}) reaches its maximum, and a weak camelback-like dispersion in the valence band (VB) and the conduction band (CB) is observed. If d_1 is further increased, the parabolic E_2 band is shifted energetically below the H_1 band. This case is shown in Fig. 2(d) (hyb2 TQW). For both cases, the electron and hole subbands are still crossing while moving away from the Γ point to finite k_{cross} [13]. Yet the inverted energy gap in the TQW is not anymore located between the H_1 level and the E_2 level but between the E_1 level and the E_2 level.

Figure 3(a) shows the extracted band-gap energies E_{gap} from the simulation data as a function of the InAs layer thickness d_1 keeping the GaSb thickness constant at $d_2 = 5.0$ nm. The crossing between the trival-insulating and the TI phases occurs at $d_1 = 9.1$ nm, while the transition between the TI phase and the gapless semimetallic phase occurs at $d_1 = 11.6$ nm. The division of the TI phase is caused by the relative position of the electron levels E_2 and E_1 with respect to the hole level H_1 as can be seen in more detail in Fig. 3(b). In the upper panel of Fig. 3(b) the position of the electronlike subbands minus the position of the H_1 band as a function

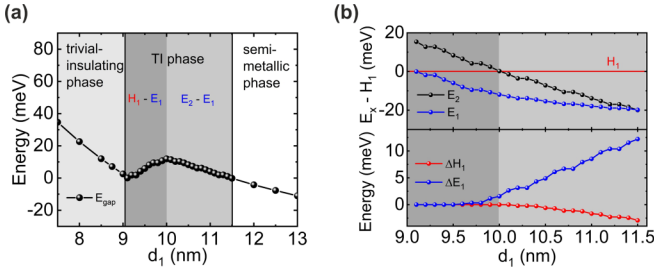


FIG. 3. (a) Extracted band-gap energies E_{gap} as a function of the InAs quantum-well thickness d_1 . The GaSb quantum-well thickness is constant ($d_2 = 5.0$ nm). (b) Upper panel: Energy values of E_2 (black) and E_1 (blue) measured against the H_1 value as a function of d_1 . Lower panel: Energy differences ΔH_1 (red) and ΔE_1 (blue) between the local energy minima and maxima in the camelback within the corresponding bands as a function of d_1 .

of d_1 is displayed. In the lower part of the TI phase (dark gray) the inverted gap opens between the H_1 - and the E_1 levels (H_1 - E_1 TI phase) and in the upper part (gray) the inverted gap opens between the E_2 - and the E_1 level (E_2 - E_1 TI phase). The dispersions of hyb1 and hyb2 shown in Figs. 2(c) and 2(d) are exemplary for the subphases. One can identify two distinct differences between the two regimes within the TI phase. For the dark gray region (H_1 - E_1 TI phase), the CB and the VB are formed by these two hybridized bands [red line for H_1 and blue dots + line for E_1 in Fig 3(b), upper panel]. This leads to a quasidirect inverted gap in this part of the TI phase, i.e., the maximum of the VB and the minimum of the CB are almost located at the same position in momentum space. As d_1 is increased above 10 nm the parabolic E_2 band is shifted energetically below the H_1 band [black dots + line in Fig. 3(b), upper panel], which results in a camelback-like dispersion only being visible for the VB, as seen in the dispersion of hyb2 in Fig. 2(d). Additionally, this can be verified by the local energy differences ΔH_1 and ΔE_1 between the energy minima and maxima of the camelback within the corresponding bands as a function of d_1 . The results are provided in the lower panel of Fig. 3(b). As the E_2 band is parabolic the local energy difference stays constant at $\Delta E_2 = 0$ meV and therefore is not shown here. For the E_1 band and H_1 band the camelback-like dispersion gets more pronounced as d_1 is increased. Note that the simulations were performed at monolayer steps with an intermediate k -space resolution to reduce computational time. Therefore, the simulation results are not completely smooth but they represent correctly the important qualitative trends.

Our samples were grown by molecular-beam epitaxy on a (001) Te- n -doped GaSb substrate, which was smoothed with a 700-nm undoped GaSb buffer. After the buffer layer, a $10 \times 2.5/2.5$ -nm AlSb/GaSb superlattice was grown. The TQWs with thicknesses as presented in Table I are sandwiched by a 40-nm-thick bottom and a top barrier consisting of the lattice-matched AlAs_{0.08}Sb_{0.92}. During growth of the TQWs Sb-soaking times of 5 s were used to create InSb-like interfaces between the TQW layers. The samples were subsequently capped with 5 nm GaSb. Hall bars of different lengths (20, 40, 60, and 80 μm) and width = 20 μm were fabricated. On top of the Hall bars we used a $5 \times 10/10$ -nm SiO₂/Si₃N₄ superlattice as a gate dielectric and a top gate was deposited

TABLE I. Overview of the sample parameters with the numerically calculated energy gap values.

| Sample | d_1 (InAs) (nm) | d_2 (GaSb) (nm) | E_{gap} (meV) |
|---------------|-------------------|-------------------|------------------------|
| triv (green) | 8.0 | 5.0 | 22.6 |
| hyb1 (blue) | 10.0 | 5.0 | 11.0 |
| hyb2 (yellow) | 10.75 | 5.0 | 6.7 |
| sm (red) | 13.5 | 5.0 | |

consisting of 60 nm Cr and 250 nm Au. If not stated otherwise, all measurements were performed at $T = 4.2$ K, and all measurements irrespective of temperature were performed in the dark.

Figure 4 shows the longitudinal resistivity ρ_{xx} of the four samples as a function of the top-gate voltage V_{TG} at $B = 0$ T. The voltage values are normalized to the charge-neutrality point (V_{CNP}). All Hall bars shown in this figure have a width of 20 μm and a length of 40 μm . For large positive gate voltages, the Fermi energy is in the electron regime and for large negative voltages it is in the hole regime. Due to the higher mobility of electrons compared to holes, ρ_{xx} in the hole regime is much larger compared to the electron regime. The triv sample [panel (a)] shows a peak in ρ_{xx} at 8.5 k Ω . Figure 4(b) displays the ρ_{xx} trace of the gapless semimetallic sample. Indeed, no resistance peak is observed as ρ_{xx} increases starting at 210 Ω at $V_{\text{TG}} - V_{\text{CNP}} = 6.5$ V and then saturates at values of around 680 Ω . The maximum resistivity values for hyb1 [Fig. 4(c)] and hyb2 [Fig. 4(d)] are 7.5 and

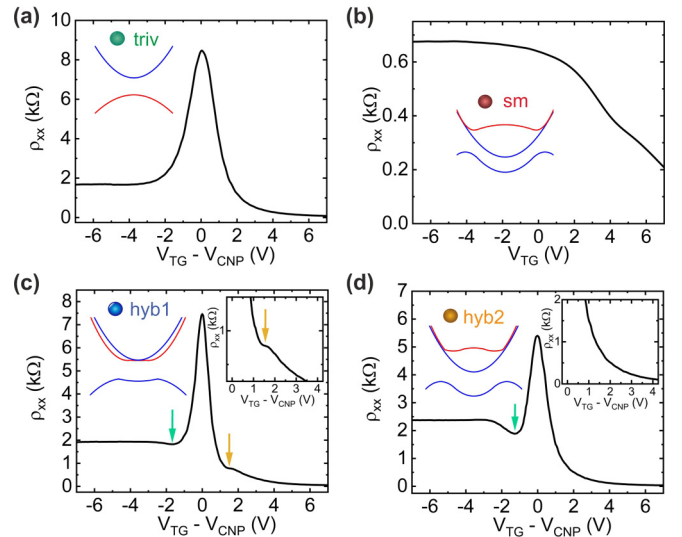


FIG. 4. Gate-voltage traces of the longitudinal resistivity for the trivial, the sm, the hyb1, and the hyb2 sample in (a), (b), (c), and (d), respectively. (a) Trivial sample: E_F is in the electron regime for gate voltages above V_{CNP} and in the hole regime for voltages below V_{CNP} . (b) sm sample: The semimetallic sample shows a gapless resistance trace. The ρ_{xx} values are significantly lower compared to all other samples. (c) hyb1 sample: VHS are observable for the CB and VB due to a camelback-like dispersion in both bands and a gap is observed. (d) hyb2 sample: a VHS is only observable in the hole regime due to the camelback-like dispersion only in the VB. The VHS is much more pronounced compared to the hyb1 sample.

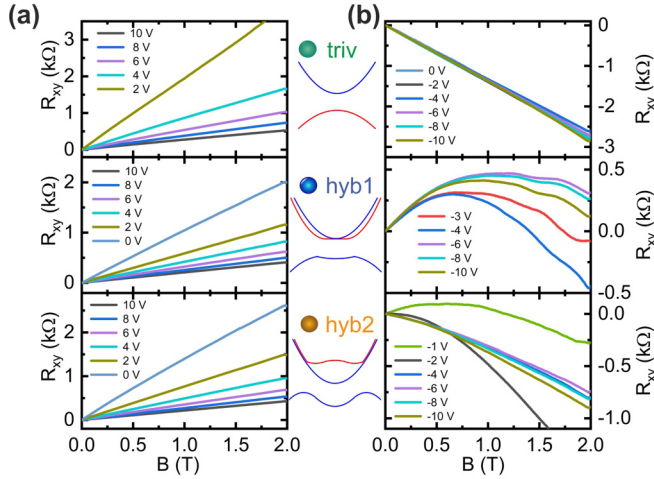


FIG. 5. Hall resistance of the triv, hyb1, and hyb2 sample in (a) the electron regime and the gap and the (b) hole regime for magnetic fields up to 2 T. The Hall resistance traces of the trivial sample are evolving linearly for both regimes, whereas the traces for both hybridized samples are only linear in the electron regime. In the gap and hole regime, a nonlinearity in R_{xy} can be seen for hyb1 and hyb2.

5.4 k Ω , respectively. The ρ_{xx} trace of the hyb1 sample shows two distinct differences compared to the resistivity trace of the trivial sample. On both sides of the resistivity peak, local minima marked by the green and the orange arrows can be observed. These features are related to the VHS [16,23–25]. The occurrence of a VHS in the conduction- and valence bands is a clear signature of the hybridized camelback-like band dispersion in both bands [see Fig. 2(c)]. In comparison, the ρ_{xx} trace for the hyb2 TQW shows just one VHS on the left side of the resistivity peak (see green arrow), i.e., in the valence band, as seen in Fig. 4(d), although the minimum is much more pronounced compared to sample hyb1. As shown in Fig. 2(d), the camelback of the hyb2 sample occurs only in the VB. The energy difference ΔE_1 of the camelback has a value of 6.5 meV for sample hyb2 compared to 1.5 meV for sample hyb1 [see Fig. 3(b), bottom panel], which is in good agreement with the differently pronounced minima of ρ_{xx} in the measured samples.

Figure 5 shows the Hall resistance R_{xy} of the three samples triv, hyb1 and hyb2 for magnetic fields up to $B = 2$ T. The left panel (a) corresponds to the electron regime and the right panel (b) to the gap and hole regime. Between both panels, the dispersion for the respective sample is displayed. For the triv sample, the Hall resistance is linear for both regimes as expected due to the single charge-carrier transport. The Hall traces for the hybridized samples hyb1 show linear Hall resistance traces deep in the electron regime (gate voltages greater than 2 V) but nonlinear Hall resistances in the gap regime and hole regime. Within the hole regime, still a prominent minority electron contribution can be observed. For the hyb2 sample, the Hall traces show again a linear dependency for gate voltages above $V_{TG} > 0$ V and are nonlinear for voltages below. In the hole regime though, a smaller minority electron contribution is observed and therefore the Hall traces evolve nearly linearly for larger negative V_{TG} .

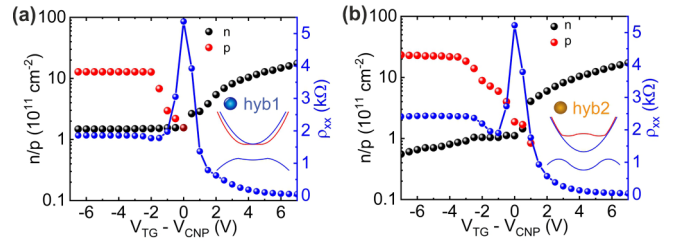


FIG. 6. Charge-carrier densities from the two-carrier fitting for the hyb1 and the hyb2 sample in (a) and (b), respectively. The corresponding longitudinal resistivity ρ_{xx} at $B = 0$ T is also shown in blue. The electron densities decrease with decreasing gate voltages for both samples. For both samples a minority electron density is observable in the gap and hole regime due to the hybridized band structure.

We evaluate the charge-carrier densities in the different regimes from the Hall resistances via a two-carrier fitting [2] for the two TI samples as shown in Fig. 6 (the data for the triv sample are not depicted here as it displays a single-carrier behavior). The corresponding ρ_{xx} traces are plotted in blue. Both samples show a comparable electron density ($n_{\text{hyb1}} = 17.6 \times 10^{11} \text{ cm}^{-2}$ and $n_{\text{hyb2}} = 17.3 \times 10^{11} \text{ cm}^{-2}$ at $V_{TG} = 6.5$ V) for gate voltages much greater than V_{CNP} . The corresponding mobilities are $\mu_{e,\text{hyb1}} = 7.3 \times 10^4 \text{ cm}^2/\text{Vs}$ and $\mu_{e,\text{hyb2}} = 8.6 \times 10^4 \text{ cm}^2/\text{Vs}$, respectively. The electron density decreases linearly with decreasing gate voltages. In the gap region the hole density starts to increase. Around V_{CNP} the electron and hole density are nearly equal with $n_{CNP} \approx p_{CNP} \approx 1.56 \times 10^{11} \text{ cm}^{-2}$ for sample hyb1 and $1.89 \times 10^{11} \text{ cm}^{-2}$ for sample hyb2. The crossing of the electron and hole bands can be calculated out of these values via $k_{\text{cross}} = \sqrt{2\pi n_{CNP}}$. This leads to crossing values $k_{\text{cross,hyb1}} \approx 0.10 \times 10^9 \text{ m}^{-1}$ and $k_{\text{cross,hyb2}} \approx 0.11 \times 10^9 \text{ m}^{-1}$, which are consistent with the simulations. For the hyb1 sample the electron and hole densities saturate for negative V_{TG} at values around $p = 12.8 \times 10^{11} \text{ cm}^{-2}$ and $n = 1.5 \times 10^{11} \text{ cm}^{-2}$ due to Fermi-level pinning. For the hyb2 sample we see a slight increase in the hole carrier density and a decrease in the electron carrier density for negative gate voltages deep in the hole regime. Furthermore, it can be seen that the hole density in the hyb1 sample with $p = 12.8 \times 10^{11} \text{ cm}^{-2}$ is around a factor of 2 smaller compared to $p = 22.9 \times 10^{11} \text{ cm}^{-2}$ in the hyb2 sample. At the same time the electron density in the VB is around a factor of 2–3 higher in the hyb1 sample compared to $n_{\text{hyb2}} = 0.55 \times 10^{11} \text{ cm}^{-2}$ for sample hyb2. We attribute this feature to the different camelback-like dispersions as shown in Figs. 2(c) and 2(d) for hyb1 and hyb2, respectively. As the dispersions illustrate, the curvature of the hybridized part in the H_1 band in hyb2 is stronger than for hyb1. This leads to different effective masses for the electrons ($m_{e,\text{hyb1}}^* > m_{e,\text{hyb2}}^*$) in the H_1 band. This directly corresponds to the difference in the density of states, which explains the higher electron density in the VB for hyb1 in comparison to hyb2 [26].

To determine the energy and nature (trivial/hybridized) of the gap for the triv, hyb1, and hyb2 sample, temperature-dependent measurements were performed. Figures 7(a)–7(c) show the gate-voltage dependent ρ_{xx} of the samples triv, hyb1, and hyb2 at temperatures from 4.2 to 65 K. With increasing

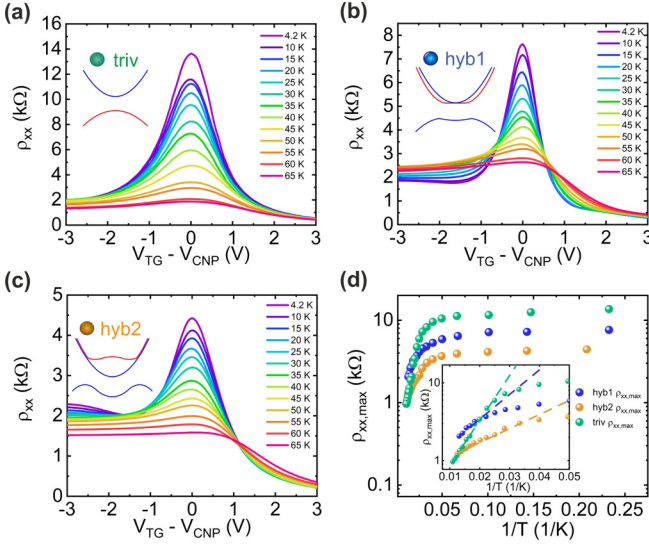


FIG. 7. (a) V_{TG} dependency of ρ_{xx} at different temperatures (color coded) starting from $T = 4.2$ K for the trivial, the hyb1, and the hyb2 sample in (a), (b), and (c). With increasing temperature, the resistivity peak corresponding to the trivial/inverted gap reduces until it vanishes at higher temperatures. (d) Arrhenius plot of the temperature dependence of the peak resistivity $\rho_{xx,max}$ for the three samples triv, hyb1, and hyb2. The inset shows the data in the high-temperature regime. The dashed lines are fits with a single-exponential function to extract the energy gap values.

temperature, the peak value of the resistivity $\rho_{xx,max}$ decreases for all samples until it vanishes at higher temperatures. The decrease of the gap resistance values shows the insulating character [11]. The extracted values for $\rho_{xx,max}$ versus the inverse temperature are plotted in Fig. 7(d). $\rho_{xx,max}$ data values are color coded as stated previously. The inset in Fig. 7(d) shows a zoom-in of the data curves to highlight the values at higher temperatures. To extract E_{gap} for the samples, the high-temperature data are fitted with a single-exponential function, given by $(\rho_{xx,max})^{-1} = A_1 \times \exp(-\frac{E_A}{2k_b T}) + A_0$, where k_b is the Boltzmann constant and A_i ($i = 0, 1$) are constants with the dimensions of conductivity. The activation energy E_A corresponds to E_{gap} in the samples. The dashed lines in Fig. 7(d) show the fitting curves, and the extracted data are summarized in Table II. A single-exponential fit for the high-temperature regime is sufficient to extract the gap energies and routinely used in the literature as well [5,25], although, as presented by Irie *et al.* [11], a double-exponential fitting may allow to get more insights in the activation

TABLE II. Overview of the energy gap values E_{gap} from the numerical calculations ($E_{gap,sim}$) and the calculated gap values ($E_{gap,exp}$) from the single-exponential fit shown in Fig. 6(d) with their respective errors.

| Sample | $E_{gap,sim}$ (meV) | $E_{gap,exp}$ (data) |
|---------------|---------------------|----------------------|
| triv (green) | 22.6 | 23 ± 2 meV |
| hyb1 (blue) | 11.0 | 11 ± 1 meV |
| hyb2 (yellow) | 6.7 | 7 ± 1 meV |

of different channels (e.g., localization energy). We also performed such double-exponential fitting and extract gap energies of $E_{gap,triv} = 22.98$ meV, $E_{gap,hyb1} = 18.65$ meV, and $E_{gap,hyb2} = 6.63$ meV. One can see that $E_{gap,triv}$ and $E_{gap,hyb2}$ agree reasonably well but $E_{gap,hyb1}$ is overestimated, although we observe that the values for the localization energy (expected in the low-meV range) are too high and in the range of a few meV. We thus see that the extraction of the localization energy is highly erroneous. One explanation is the temperature limitation in the experiment (i.e., above 4 K) and to accurately determine the localization energy (and also E_{gap}) lower temperatures are needed. We therefore conclude that for extracting the gap energies from our measurements the single-exponential fit is most suitable. For the trivial TQW we obtain a band-gap energy of $E_{gap,triv} = (23 \pm 2)$ meV. For the hybridized TQWs we extracted hybridization band-gap values of $E_{gap,hyb1} = (11 \pm 1)$ meV and $E_{gap,hyb2} = (7 \pm 1)$ meV. These gap values are in good agreement with the simulated data. Although the band gap of the trivial sample is about 2–3 times larger compared to the hyb1 and hyb2 samples, all resistivity peaks vanish at similar temperatures (~ 75 K). These measurement data from the temperature series point to a rather temperature-insensitive inverted gap for the hyb1 and hyb2 sample [19,20,22].

III. CONCLUSIONS

In summary, we have presented an experimental investigation of the phase diagram for symmetrically grown InAs/GaSb/InAs TQW samples. Our findings allow to better understand the TI phase with their fine graduation into H_1 - E_1 and E_2 - E_1 TI phase. The exploration of the phase diagram and especially a deeper understanding of the evolution of the dispersions is a useful step towards the development of a topological device from this material system. We performed gate-voltage dependent magnetotransport and temperature-dependent measurements of TQW samples located in the different regimes of the phase diagram, especially with two TQW samples located in the two different subparts of the TI phase. We observed two Van Hove singularities, one in the valence band and one in the conduction band, for the sample located in the quasidirect H_1 - E_1 TI phase and one Van Hove singularity in the valence band for the sample located in the indirect E_2 - E_1 TI phase due to the hybridized electron-hole band structure. We discussed in detail the reasons for the appearance and the number of the Van Hove singularities in connection with the theoretical relative positions of the E_1 , E_2 , and H_1 bands and the differences appearing in the numerical dispersions. We studied the charge-carrier density evolution and the two-carrier behavior in the hybridized samples due to the coexistence of electrons and holes. Thus, we demonstrate the hybridized topological band structure of those samples. Additionally, we could provide information about samples located in the trivial-insulating and the semimetallic phase, which delivers a full experimental exploration of the TQW phase diagram. Finally, we studied the evolution of the band-gap energy for the trivial- and the two hybridized samples via temperature-dependent measurements and calculated the band-gap energy for the different samples. We have evidenced a more temperature-insensitive behavior of the two inverted

gaps for the hybridized samples in comparison to the energy gap in the trivial sample. This behavior could in the future enable operations at higher temperatures, which are necessary for the development of topological devices.

ACKNOWLEDGEMENTS

The work was supported by the Elite Network of Bavaria within the graduate program “Topological Insulators.” Expert technical assistance by A. Wolf is gratefully acknowledged.

-
- [1] C. Liu, T. L. Hughes, X. L. Qi, K. Wang, and S. C. Zhang, Quantum Spin Hall Effect in Inverted Type-II Semiconductors, *Phys. Rev. Lett.* **100**, 236601 (2008).
- [2] F. Qu, A. J. A. Beukman, S. Nadj-Perge, M. Wimmer, B.-M. Nguyen, W. Yi, J. Thorp, M. Sokolich, A. A. Kiselev, M. J. Manfra, C. M. Marcus, and L. P. Kouwenhoven, Electric and Magnetic Tuning between the Trivial and Topological Phases in InAs/GaSb Double Quantum Wells, *Phys. Rev. Lett.* **115**, 036803 (2015).
- [3] F. Nichele, A. N. Pal, P. Pietsch, T. Ihn, K. Ensslin, C. Charpentier, and W. Wegscheider, Insulating State and Giant Nonlocal Response in an InAs/GaSb Quantum Well in the Quantum Hall Regime, *Phys. Rev. Lett.* **112**, 036802 (2014).
- [4] M. Karalic, C. Mittag, S. Mueller, T. Tschirky, W. Wegscheider, K. Ensslin, T. Ihn, and L. Glazman, Phase slips and parity jumps in quantum oscillations of inverted InAs/GaSb quantum wells, *Phys. Rev. B* **99**, 201402(R) (2019).
- [5] L. Du, T. Li, W. Lou, X. Wu, X. Liu, Z. Han, C. Zhang, G. Sullivan, A. Ikhlassi, K. Chang, and R. R. Du, Tuning Edge States in Strained-Layer InAs/GaInSb Quantum Spin Hall Insulators, *Phys. Rev. Lett.* **119**, 056803 (2017).
- [6] I. Knez, R. R. Du, and G. Sullivan, Finite conductivity in mesoscopic Hall bars of inverted InAs/GaSb quantum wells, *Phys. Rev. B* **81**, 201301(R) (2010).
- [7] V. S. Pribiag, A. J. A. Beukman, F. Qu, M. C. Cassidy, C. Charpentier, W. Wegscheider, and L. P. Kouwenhoven, Edge-mode superconductivity in a two-dimensional topological insulator, *Nat. Nanotechnol.* **10**, 593 (2015).
- [8] E. M. Spanton, K. C. Nowack, L. Du, G. Sullivan, R. R. Du, and K. A. Moler, Images of Edge Current in InAs/GaSb Quantum Wells, *Phys. Rev. Lett.* **113**, 026804 (2014).
- [9] G. Knebl, P. Pfeffer, S. Schmid, M. Kamp, G. Bastard, E. Batke, L. Worschech, F. Hartmann, and S. Höfling, Optical tuning of the charge carrier type in the topological regime of InAs/GaSb quantum wells, *Phys. Rev. B* **98**, 041301(R) (2018).
- [10] M. König, L. W. Molenkamp, X. Qi, and S. Zhang, Quantum spin Hall insulator state in HgTe quantum wells, *Science* **318**, 766 (2007).
- [11] H. Irie, T. Akiho, F. Couëdo, K. Suzuki, K. Onomitsu, and K. Muraki, Energy gap tuning and gate-controlled topological phase transition in InAs/InxGa1-xSb composite quantum wells, *Phys. Rev. Mater.* **4**, 104201 (2020).
- [12] P. Leubner, L. Lunczer, C. Brüne, H. Buhmann, and L. W. Molenkamp, Strain Engineering of the Band Gap of HgTe Quantum Wells Using Superlattice Virtual Substrates, *Phys. Rev. Lett.* **117**, 086403 (2016).
- [13] S. S. Krishtopenko and F. Teppe, Quantum spin Hall insulator with a large bandgap, Dirac fermions, and bilayer graphene analog, *Sci. Adv.* **4**, eaap7529 (2018).
- [14] M. Marcinkiewicz, S. Ruffenach, S. S. Krishtopenko, A. M. Kadykov, C. Consejo, D. B. But, W. Desrat, W. Knap, J. Torres, A. V. Ikonnikov, K. E. Spirin, S. V. Morozov, V. I. Gavrilenko, N. N. Mikhailov, S. A. Dvoretiskii, and F. Teppe, Temperature-driven single-valley Dirac fermions in HgTe quantum wells, *Phys. Rev. B* **96**, 035405 (2017).
- [15] S. Wiedmann, A. Jost, C. Thienel, C. Brüne, P. Leubner, H. Buhmann, L. W. Molenkamp, J. C. Maan, and U. Zeitler, Temperature-Driven Transition from a Semiconductor to a Topological Insulator, *Phys. Rev. B* **91**, 205311 (2015).
- [16] M. Meyer, S. Schmid, F. Jabeen, G. Bastard, F. Hartmann, and S. Höfling, Topological band structure in InAs/GaSb/InAs triple quantum wells, *Phys. Rev. B* **104**, 085301 (2021).
- [17] S. S. Krishtopenko, W. Desrat, K. E. Spirin, C. Consejo, S. Ruffenach, F. Gonzalez-Posada, B. Jouault, W. Knap, K. V. Maremyanin, V. I. Gavrilenko, G. Boissier, J. Torres, M. Zakoune, E. Tournié, and F. Teppe, Massless Dirac fermions in III-V semiconductor quantum wells, *Phys. Rev. B* **99**, 121405(R) (2019).
- [18] S. S. Krishtopenko, S. Ruffenach, F. Gonzalez-Posada, G. Boissier, M. Marcinkiewicz, M. A. Fadeev, A. M. Kadykov, V. V. Romyantsev, S. V. Morozov, V. I. Gavrilenko, C. Consejo, W. Desrat, B. Jouault, W. Knap, E. Tournié, and F. Teppe, Temperature-dependent terahertz spectroscopy of inverted-band three-layer InAs/GaSb/InAs quantum well, *Phys. Rev. B* **97**, 245419 (2018).
- [19] S. S. Krishtopenko, S. Ruffenach, F. Gonzalez-Posada, C. Consejo, W. Desrat, B. Jouault, W. Knap, M. A. Fadeev, A. M. Kadykov, V. V. Romyantsev, S. V. Morozov, G. Boissier, E. Tournié, V. I. Gavrilenko, and F. Teppe, Terahertz spectroscopy of two-dimensional semimetal in three-layer InAs/GaSb/InAs quantum well, *JETP Lett.* **109**, 96 (2019).
- [20] I. Vurgaftman, J. R. Meyer, and L. R. Ram-Mohan, Band parameters for III-V compound semiconductors and their alloys, *J. Appl. Phys.* **89**, 5815 (2001).
- [21] H. Kroemer, The 6.1 Å family (InAs, GaSb, AlSb) and its heterostructures: A selective review, *Phys. E (Amsterdam, Neth.)* **20**, 196 (2004).
- [22] See <https://www.nextnano.de/index.php> for NEXTNANO.
- [23] I. Brihuela, P. Mallet, H. González-Herrero, G. Trambly De Laissardière, M. M. Ugeda, L. Magaud, J. M. Gómez-Rodríguez, F. Ynduráin, and J. Y. Veillen, Unraveling the Intrinsic and Robust Nature of Van Hove Singularities in Twisted Bilayer Graphene by Scanning Tunneling Microscopy and Theoretical Analysis, *Phys. Rev. Lett.* **109**, 196802 (2012).
- [24] M. J. Yang, C. H. Yang, B. R. Bennett, and B. V. Shanabrook, Evidence of a Hybridization Gap in “Semimetallic” InAs/GaSb Systems, *Phys. Rev. Lett.* **78**, 4613 (1997).
- [25] M. Karalic, S. Mueller, C. Mittag, K. Pakrouski, Q. S. Wu, A. A. Soluyanov, M. Troyer, T. Tschirky, W. Wegscheider, K. Ensslin, and T. Ihn, Experimental signatures of the inverted phase in InAs/GaSb coupled quantum wells, *Phys. Rev. B* **94**, 241402(R) (2016).
- [26] E. Yamaguchi, Electron subbands and transport properties in inversion layers of InAs and InP, *Phys. Rev. B* **32**, 5280 (1985).